This is a preprint, the final version is subject to change, of the American Mineralogist (MSA)
Cite as Authors (Year) Title. American Mineralogist, in press.
DOI: https://doi.org/10.2138/am-2020-7379

Revision 1

Evaluation and application of the quartz-inclusions-in-epidote mineral barometer

Miguel Cisneros[1,2]*, Kyle T. Ashley[3], and Robert J. Bodnar[4]

[1]*Current address: Structural Geology and Tectonics Group, Geological Institute, Department of Earth Sciences, ETH Zürich, Sonneggstrasse 5, Zürich, 8092, Switzerland*

[2]*Previous address: Department of Geological Sciences, Jackson School of Geosciences, University of Texas at Austin, 2275 Speedway Stop C9000, Austin, TX 78712, USA*

[3]*Department of Geology and Environmental Science, University of Pittsburgh, 4107 O'Hara Street, Pittsburgh, PA 15260, USA*

[4] *Department of Geosciences, Virginia Tech, 4044 Derring Hall (0420), Blacksburg, VA 24061, USA*

**Corresponding author (e-mail: miguel.cisneros@erdw.ethz.ch)*

Abstract

We have examined the suitability of a quartz-inclusions-in-epidote (qtz-in-ep) mineral barometer to better constrain P-T histories of epidote-bearing lithologies. Theoretical calculations applying an isotropic elastic model suggest that the qtz-in-ep barometer exhibits minimal temperature dependence, and thus, offers the potential to constrain growth conditions of epidote in various geologic environments, including skarn deposits, epidote-bearing granitoids, and metamorphic rocks.

This is a preprint, the final version is subject to change, of the American Mineralogist (MSA)
Cite as Authors (Year) Title. American Mineralogist, in press.
DOI: https://doi.org/10.2138/am-2020-7379

To test if the applied equations of state and isotropic elastic model reasonably simulate the elastic evolution of two anisotropic minerals, we measured Raman shifts of the 464 cm^{-1} band of quartz inclusions relative to that of an unencapsulated quartz standard. We calculated a quartz inclusion pressure (P_{incl}^{464}) at various temperatures, and compared these values with temperature-dependent P_{incl} predicted by elastic modeling (P_{incl}^{mod}) at elevated temperatures. Three epidote-bearing samples with reasonably well-constrained P-T histories were also examined: 1) sample HF14C from the Upper Schieferhuelle in the Western Tauern Window (P_{incl}^{464} = 0.01 GPa), 2) sample LdC-31C from Lago di Cignana ($P_{incl}^{464} \approx$ 0.16 GPa), and 3) sample FT1E from the Frosnitz Tal in the Western Tauern region (P_{incl}^{464} = 0.57 GPa).

Entrapment pressures (P_{ent}^{464}) calculated from P_{incl}^{464} determined at various temperatures show nominal differences from P_{ent} calculated from P_{incl}^{mod}, suggesting that for qtz-in-ep pairs, the calculated P_{ent} does not significantly vary with the temperature of measurement. Furthermore, our calculated P_{ent}^{464} for a sample from the Upper Schieferhuelle is in agreement with petrographic context and previously-established P conditions, and the P_{ent}^{464} determined for the Frosnitz Tal sample closely approximate previously reported pressures. The Lago di Cignana sample is derived from an epidote vein that is encased in a high-P foliation, and the calculated P_{ent}^{464} is consistent with early, low-P epidote vein formation that pre-dates high-P metamorphism, or alternatively, late vein formation during exhumation, and confirms that the epidote did not form at or near peak conditions (~2.0 GPa). Results of this study indicate that the qtz-in-ep barometer potentially provides another tool that geoscientists can employ to better constrain P-T conditions in some epidote-bearing environments, where conventional thermobarometric techniques cannot be applied.

Introduction

This is a preprint, the final version is subject to change, of the American Mineralogist (MSA)
Cite as Authors (Year) Title. American Mineralogist, in press.
DOI: https://doi.org/10.2138/am-2020-7379

A fundamental goal of many geosciences studies is to constrain the pressure-temperature (P-T) histories of igneous and metamorphic rocks. Many different thermobarometers have been developed during the past decades to unravel complex P-T histories, and in recent years, elastic thermobarometry has gained wide acceptance and applicability. Elastic thermobarometry is a method that can constrain P-T conditions in a wide range of geologic environments, and records conditions at which a host crystal grows and encapsulates a mineral inclusion. Because the elastic properties of the inclusion and host almost always differ, upon exhumation an inclusion can develop a residual pressure that is higher (or lower) than that of the surrounding host. Application of elastic thermobarometers requires that changes in inclusion and host volumes from the time of host growth through exhumation to Earth's surface are well constrained. When combined with careful petrographic, mineralogical and petrological studies, the method can be applied to constrain P-T conditions of mineral growth and fabric development, allowing deformation and tectonic processes to be independently constrained. The potential applications of the technique are many, yet the applicability of the technique has been limited to a few inclusion-host pairs, such as apatite-in-garnet (Ashley et al. 2017; Barkoff et al. 2017, 2019), quartz-in-garnet (e.g., Enami et al. 2007; Ashley et al. 2014, 2015; Kouketsu et al. 2014; Spear et al. 2014; Behr et al. 2018; Bonazzi et al. 2019), zircon-in-garnet (Zhong et al. 2019), garnet-in-diamond (Kueter et al. 2016), kyanite-in-diamond (Nestola et al. 2018), magnesiochromite-in-diamond (Nestola et al. 2019), olivine-in-diamond (Izraeli et al. 1999; Nestola et al. 2011; Howell et al. 2012), periclase-in-diamond (Anzolini et al. 2019), and coesite-in-diamond, garnet, and zircon (Parkinson and Katayama 1999; Sobolev et al. 2000). The quartz-in-garnet (qtz-in-grt) inclusion-host pair is the most commonly implemented barometer because the high compressibility of quartz relative to the rigid host garnet allows for retention of significant residual pressures. Additionally, the ubiquity

of quartz inclusions in garnet, the stability of garnet across a wide range of P-T conditions, and the fact that garnet is a nearly isotropic host, makes this technique applicable to a wide range of geologic environments.

Quartz-in-epidote (qtz-in-ep) is similarly a potentially useful barometer because: 1) the qtz-in-ep barometer exhibits minimal temperature dependence (Fig. 1); 2) epidote is abundant and crystallizes in a broad range of geologic settings (P-T conditions); 3) quartz is commonly found as inclusions within epidote in a wide range of rock types; and 4) the thermodynamic properties of quartz and epidote group minerals are reasonably well constrained (e.g., Holland et al. 1996; Pawley et al. 1996; Mao et al. 2007; Gatta et al. 2011; Qin et al. 2016). The barometer is not limited by sluggish kinetics and partial disequilibrium (e.g., Rubie 1998; Carlson 2002), and can help to constrain P-T conditions that other thermobarometers may fail to record (e.g., fluid inclusions are commonly modified or destroyed during prograde metamorphism). The qtz-in-ep barometer offers the potential to constrain formation conditions in several environments for which few other barometers are available, including epidote-bearing skarn deposits, epidote-bearing granitoids, metamorphic rocks, epidote veins, and hydrothermally altered igneous rocks. The qtz-in-ep barometer, combined with detailed field observations, examination of microstructures and petrographic relationships, and independent thermobarometry, offers the possibility to considerably improve our understanding of the P-T history of epidote-bearing rocks. The qtz-in-ep barometer can potentially refine estimates of depths (pressures) of epidote formation in metamorphic rocks and can be applied to a wide-range of bulk compositions, and the barometer can also supplement existing techniques to determine formation conditions of epidote-bearing granitoids and skarns.

This study describes the applicability of a qtz-in-ep barometer by measuring temperature dependent Raman band positions of quartz, and comparing entrapment pressures calculated from elastic thermobarometry with independent thermobarometry (Selverstone and Spear 1985; Selverstone et al. 1992; Frezzotti et al. 2011). We follow a similar approach to that implemented by Ashley et al. (2016). Elastic models have been developed for isotropic minerals and assume a spherical inclusion geometry, and experiments that determine pressure-dependent Raman shifts are carried out under hydrostatic conditions. For the quartz-in-epidote pair, these assumptions may not be appropriate, necessitating the need for heating measurements to monitor the inclusion pressure of the inclusion-host pair as temperature changes. Therefore, Raman analyses were conducted at various temperatures to test the ability of the current modeling approach to predict the evolution of inclusion pressure during heating of two anisotropic minerals (quartz-in-epidote). We compare heating measurements and model results by two methods: 1) the Raman shift of the quartz 464 cm^{-1} band was measured and used to calculate an inclusion pressure (P_{incl}^{464}) at a given temperature, which we compared to P_{incl} that is predicted by elastic modeling at elevated temperatures (P_{ent}^{mod}), and 2) entrapment pressures (P_{ent}^{464}) are calculated based on P_{incl}^{464} at elevated temperature and are compared to entrapment pressures calculated from P_{ent}^{mod}.

Samples

Quartz inclusions in epidote from three samples with well-constrained P-T histories were analyzed, and we compared our pressure estimates to the previously-determined P-T histories. The samples are from three different localities that have experienced different P-T histories, and they allow us to test the feasibility of implementing the qtz-in-ep barometer in metamorphic rocks that have experienced different P-T paths. We also consider whether our calculated entrapment

pressures are reasonable and consistent with the petrographic evidence that documents the formation and deformation history of the epidote hosts.

Upper Schierferhuelle – HF14C

Sample HF14C is a metamafic rock from the Upper Schieferhuelle (USH) in the western Tauern Window, Italy, that contains a well-defined foliation defined by amphibole, epidote, quartz, chlorite, and plagioclase. P-T estimates that are used here for comparison have been derived from pelitic and mafic samples in the USH.

Reference P-T conditions of USH pelites have been estimated based on (1) mineral chemistry thermobarometry, (2) Gibbs modeling of garnet zoning, and (3) fluid-inclusion thermobarometry (Ferry and Spear 1978; Spear and Selverstone 1983; Selverstone and Spear 1985). Garnet-biotite thermometry, and garnet-plagioclase-biotite-muscovite barometry (from garnet rims and matrix grain rims) give P-T estimates of ~475 ± 25 ºC and ~ 0.5 – 0.6 GPa. Garnet core and rim modeling indicate P-T conditions of ~ 450 ºC and ~0.5 – 0.6 GPa, and ~ 475 ºC and ~0.5 – 0.6 GPa, respectively. Garnet zoning between cores and rims indicates intermittent pressure fluctuations during heating. The texturally oldest fluid inclusions in this sample indicate P-T conditions of ~0.6 GPa and ~450 – 500 °C and may record near peak (T) conditions or the early stages of USH exhumation. Younger fluid inclusions indicate near isothermal decompression after the USH reached peak P-T conditions.

P-T constraints for the mafic samples from the Upper Schieferhuelle (USH) are based on a lack of glaucophane, the presence of lawsonite pseudomorphs, and the stability of Ca-amphibole, albite, and chlorite throughout the history of the mafic samples, which places P-T conditions in a field that has been described as the lawsonite-albite-chlorite subfacies of blueschist facies (~0.4 -

0.6 GPa; Turner 1981; Selverstone and Spear 1985; Peacock 1993). Epidotes from this sample are oriented parallel to foliation and suggest that growth of epidote occurred prior to, or during, foliation-forming deformation (Fig. 2A) – this observation is important for comparing our results with previous P-T estimates, as described in more detail below.

Lago di Cignana – LdC-31C

Sample LdC-31C (SESAR database; hand sample: IGSN = IECHL005C, thin section: IGSN = IECHL00B2) is a felsic rock from Lago di Cignana, Italy (Selverstone and Sharp 2013), a region that has experienced ultra-high-pressure metamorphism as evidenced by a diamond-bearing horizon (Frezzotti et al. 2011). Temperature estimates of ~600 ºC, with minimum pressure estimates of 3.2 – 3.4 GPa, suggest that these samples reached the diamond stability field where quartz is not stable (Groppo et al. 2009; Frezzotti et al. 2011). The foliation in the rock is defined by quartz, epidote and white mica; however, epidote that we analyzed is derived from a coarse-grained epidote-fuchsite vein that exhibits an irregular, undulating contact with the primary foliation (Fig. 2B). The undulating boundary suggests that the epidote in the vein may have formed prior to the primary foliation-forming event in the region, or during exhumation, and experienced minor deformation after formation of the primary foliation.

Frosnitz Tal – FT1E

Sample FT1E is a metasediment from Frosnitz Tal in the Tauern Window, Austria, that contains a well-defined foliation defined by quartz, epidote, white mica, omphacite, and chlorite (Fig. 2C). Most published P-T conditions for the area are derived from metabasites from the eclogite zone, and indicate peak metamorphic conditions of ~ 625 ºC and ~1.9 – 2.5 GPa, based on multiple thermobarometric techniques, e.g., Holland (1979): 650 C, 1.95 GPa; Selverstone et

al. (1992): 625 °C, 2.0 GPa; Kurz et al. (1998): 550 – 635 °C, 1.9 – 2.3 GPa; Hoschek (2001): 590-630 °C, 1.95 – 2.24 GPa; Miller and Konzett (2003): 623 °C, 2.04 GPa; Hoschek (2007): 630 °C, 2.5 GPa. Slightly lower peak P-T conditions (P ≈ 2.0 GPa, T ≈ 600 °C) have been estimated for adjacent metasediments (e.g., Spear and Franz 1986). Epidotes in the matrix are oriented parallel to the primary foliation, suggesting crystallization of epidote occurred prior to, or during, the primary fabric forming deformation.

Analytical methods

To test the suitability of using an isotropic elastic model to interpret data obtained from two anisotropic phases, quartz inclusions in epidotes from three localities were analyzed by Raman spectroscopy at various temperatures. For samples HF14C and FT1E, a single quartz inclusion in epidote was analyzed. During heating and analysis of a quartz inclusion in sample LdC-31C, the window in the heating stage cracked and the inclusion could not be heated to the final temperature; a second inclusion in a different epidote crystal from this sample was selected and analyzed. Samples were prepared by doubly polishing single epidote crystals that were then individually loaded onto a heating stage for Raman analyses. The diameter of measured quartz inclusions ranged from 10 – 15 μm, and significant care was taken to select isolated inclusions that were away from recognizable fractures, cleavage or other inclusions, and at least 3 times the inclusion radial distance from the host exterior (surface) to avoid relaxation of the inclusion (Campomenosi et al. 2018; Mazzucchelli et al. 2018).

Analyses during heating were completed at Virginia Tech on a Linkam THMSG600 heating stage mounted onto a JY Horiba LabRam HR800 Raman spectrometer with 1800 lines/mm grating. We used a 40x objective with a confocal aperture of 400 μm and a 150 μm slit width. Raman spectra were centered at 360 cm^{-1} (total spectral range of ~74 – 633 cm^{-1}). All spectra were

collected with a 514.57 nm wavelength Ar laser, 30 – 45 s accumulation time, and 3 accumulations. The laser interference filter was removed for all analyses, allowing us to simultaneously correct measurements for drift by monitoring the position of the Ar plasma lines. For all samples, Raman analyses were performed at ambient pressure and from room temperature to 600 ºC in 50 ºC increments. The inclusions were also analyzed during subsequent cooling to test for reproducibility to ensure that deformation induced during heating was elastic. All Raman spectra were temperature reduced using the Bose-Einstein distribution factor to compare Raman measurements made at elevated temperatures (Kuzmany 2009). After the spectra were temperature reduced, a linear background correction was applied to samples LdC-31C and HF14C, and a polynomial background correction was applied to sample FT1E (raw and reduced Raman spectra are provided in the Supplementary Material). All Raman data was fit using PeakFit v4.12 (by Systat Software Inc). A Gaussian area model was used to fit Ar plasma lines, and a Voigt Gaussian/Lorentz area model was used to fit quartz and adjacent epidote bands. The 116.04 and 266.29 cm^{-1}, and 520.3 cm^{-1} Ar plasma lines were used for linear drift corrections of the peak positions of quartz vibrational modes near 128 cm^{-1}, 206 cm^{-1}, and 464 cm^{-1}, respectively. Peak positions of quartz inclusion bands were determined relative to the peak positions of an unencapsulated Herkimer quartz standard that was analyzed 5 times every day during analysis of the inclusions (Table S1). The propagated errors reported in this study account for errors in peak fit statistics for the Ar plasma line, quartz peaks, and instrumental uncertainty (± 0.1 cm^{-1}).

Based on information in the RRUFF database (Lafuente et al. 2016), the Raman spectra of monoclinic epidotes shows bands in the region from ~375 – 550 cm^{-1}. Epidotes have vibrational modes that exhibit strong Raman intensities at ~ 425 cm^{-1} and 455 cm^{-1}, and lower intensity Raman modes at ~396 cm^{-1}, ~443 cm^{-1}, ~475 cm^{-1}, ~490 cm^{-1}, ~510 cm^{-1}, and ~528 cm^{-1}. The absolute

band position and intensity varies depending on composition (Fig. 3A, 3B). Furthermore, the intensity of the epidote bands varies with crystal orientation, due to the orientation-dependent polarizability of mineral vibrational modes (Fig. 3A, 3B, Graves and Gardiner 1989). To account for peak overlap, we deconvolved Raman bands that are between ~375 – 550 cm^{-1} into ~10 peaks to simultaneously fit the quartz 464 cm^{-1} band, adjacent epidote bands (~8 bands), and the 520.3 cm^{-1} Ar plasma line (Fig. 3, all high-T peak fits are provided in the Supplementary Material). The interference (overlap) of the quartz 464 cm^{-1} band with shouldering epidote bands becomes more pronounced at higher T as the quartz band shifts to lower wavenumbers and mineral peaks broaden. As epidote bands broadened at high temperature, some lower intensity bands became hidden, and they were removed from the peak fitting procedure due to the large uncertainty associated with their peak fit positions.

Electron probe microanalyses (EPMA) were carried out at the University of Texas at Austin on a JEOL 8200 microprobe equipped with five wavelength-dispersive spectrometers. Epidotes were analyzed for Na, Al, K, Mn, Ti, Mg, Si, Ca, Fe, and Cr using a 10-μm beam size, 10 nA beam current and 15 keV accelerating voltage. All elements were measured for 30 s on peak and a mean atomic number background correction was applied. Primary standards used include: synthetic anorthite glass; synthetic orthoclase; natural chromite from the Stillwater complex (531M-8); synthetic enstatite; natural Amelia albite from Amelia, Virginia; and ilmenite from the Ilmen Mountains, USSR (USNM96189). Analyses were monitored by analyzing Kakanui hornblende as a secondary standard, using the same operating conditions as for the unknowns. All iron in epidote was assumed to be ferric, and epidotes were classified according to the nomenclature of Franz and Liebscher (2004). Major element compositions of epidote hosts in this

study and the mole fractions of epidote components (epidote and clinozoisite) are given in Table S5.

Calculation procedures

Calculation of inclusion pressures

Raman shifts of the quartz (inclusion) 464 cm^{-1} band (ω^{464}_{incl}) at a given temperature were determined relative to the Raman shift of the 464 cm^{-1} band of a Herkimer quartz crystal (ω^{464}_{std}) measured at 0.1 MPa and the same temperature ($\Delta\omega^{464}_{shift} = \omega^{464}_{incl} - \omega^{464}_{std}$; Table 2). This allowed us to correct for temperature-induced strain on the quartz inclusions, and to monitor stress-induced strains (Murri et al. 2018, 2019). For sample HF14C (low-P inclusion), we calculate $\Delta\omega^{464}_{shift}$ of inclusions relative to the Herkimer quartz standard using a polynomial equation that describes the $\omega^{464}_{std}$of a Herkimer quartz analyzed at 0.1 MPa and the measurement temperature. The ω^{464}_{std}-temperature relationship is linear over most of the temperature range, but deviates from linearity near the quartz α-β transition (Fig. 4, Table S2, Ashley et al., 2016). The temperature of the quartz α-β transition occurs at ~573°C at 0.1 MPa, and increases by about 0.25°C/MPa. Thus, the higher P_{incl} samples (FT1E and LdC-31C) do not approach the quartz α-β transition during heating to 600°C, and we calculated $\Delta\omega^{464}_{shift}$ using a linear extrapolation to the polynomial equation (Fig. 4, Tables S3, S4). Quartz inclusions in epidote record a smaller change in wavenumber of the 464 cm^{-1} Raman band during heating relative to Herkimer quartz at ambient pressure, because the inclusion pressure increases during heating. The increase in $\Delta\omega^{464}_{shift}$ reflects the effect of pressure on encapsulated quartz (inclusions) during heating, due to its higher thermal expansivity relative to epidote. The hydrostatic calibration of Schmidt and Ziemann (2000) was used to calculate P^{464}_{incl} from $\Delta\omega^{464}_{shift}$ at elevated T.

Recent studies report conflicting results concerning the accuracy of entrapment pressures that are calculated from Raman shifts of the quartz 464 cm^{-1} band with increasing pressure assuming hydrostatic calibrations (P_{incl}^{464}, Thomas and Spear 2018; Bonazzi et al. 2019). Some experiments that synthesize garnets with quartz inclusions show that P_{incl}^{464} provides accurate garnet growth pressures (Thomas and Spear 2018). Results from other experiments show that sometimes P_{incl}^{464} can accurately replicate experimental conditions (2.5 GPa experiments), but that in other cases (3.0 GPa experiments), use of the 464 cm^{-1} band underestimates experimental P_{ent}, and the use of quartz strains ($P_{incl}^{strains}$) better replicates experimental conditions (± 0.2 GPa; Bonazzi et al. 2019). To assess the extent of anisotropy that quartz inclusions retain in an anisotropic host (epidote), we calculate $P_{incl}^{strains}$ to account for quartz anisotropy, and compare it to P_{incl} calculated from hydrostatic calibrations (Fig. 5, Tables S2, S3). Calculating quartz strains requires that Raman shifts of at least 2 quartz vibrational modes can be measured. For samples HF14C and LdC-31C, we measured the quartz 128, 206 and 464 cm^{-1} band positions at ambient temperature. Strains were determined from the Raman shifts of quartz 128 cm^{-1}, 206 cm^{-1} and 464 cm^{-1} bands by using Strainman (Murri et al. 2018, 2019; Angel et al. 2019), and they were then converted to a mean stress [$P_{incl}^{strains} = (2\sigma_1 + \sigma_3)/3$] using the matrix relationship $\sigma_i = c_{ij}\varepsilon_j$, where σ_i, c_{ij}, and ε_j, are the stress, elastic modulus, and strain matrices, respectively. We used the α-quartz trigonal symmetry constraints of Nye (1985) and quartz elastic constants of Wang et al. (2015). For sample FT1E, only the quartz 464 cm^{-1} band was fit at ambient temperature because the 128 and 206 cm^{-1} bands exhibited low intensities or had significant overlap with epidote peaks.

Calculation of entrapment conditions

This is a preprint, the final version is subject to change, of the American Mineralogist (MSA)
Cite as Authors (Year) Title. American Mineralogist, in press.
DOI: https://doi.org/10.2138/am-2020-7379

Entrapment pressures (P_{ent}) and modeled inclusion pressures (P_{incl}^{mod}) were calculated by implementing the Guiraud and Powell (2006) 1-D elastic model, with an updated exact solution described by Angel et al. (2017b), following the equation:

$$\left[\left(\frac{V_{Pmeas,Tmeas}}{V_{Pent,Tent}}\right)_{incl} - \left(\frac{V_{Pmeas,Tmeas}}{V_{Pent,Tent}}\right)_{host}\right]\left(\frac{V_{Pent,Tent}}{V_{Pfoot,Tmeas}}\right)_{incl} - \frac{3}{4G_{host}}(P_{incl} - P_{ext}) = 0 \quad (271)$$

Where $(V_{Pmeas,Tmeas}/V_{Pent,Tent})_{incl}$ and $(V_{Pmeas,Tmeas}/V_{Pent,Tent})_{host}$ are the molar volume ratios of the entrapped inclusion and the host at measurement conditions ($V_{Pmeas,Tmeas}$), and at entrapment conditions ($V_{Pent,Tent}$), respectively. $(V_{Pent,Tent}/V_{Pfoot,Tmeas})_{incl}$ is the inclusion molar volume ratio at entrapment conditions, and at a measurement temperature and a pressure along an isomeke defined by the entrapment conditions (V_{Pfoot}, see Angel et al. 2017b). G_{host}, P_{incl}, and P_{ext} are the shear modulus of the host, the inclusion pressure at measurement conditions, and the pressure of the host (0.1 MPa) at ambient T, respectively. P_{incl}^{mod} and P_{ent} were calculated using an internal MATLAB script that allows for ideal mixing of solid-solutions; see Table S6 for a comparison of entrapment pressures calculated using EoSFit-Pinc (Angel et al. 2017b). Modeled P_{incl} (P_{incl}^{mod}), i.e., the evolution of P_{incl} that is predicted by elastic modeling, is calculated by determining a residual quartz inclusion pressure (P_{incl}^{464}) at ambient T from Raman measurements, calculating an entrapment pressure (P_{ent}^{464}) from P_{incl}^{464} (and an assumed entrapment temperature), and subsequently back-calculating P_{incl}^{mod} at elevated T from the determined entrapment pressure (constant). Therefore, the modeled P_{ent} does not depend on the T of the Raman measurement. The increase of P_{incl}^{mod} reflects the increase in pressure that an inclusion would have to record at elevated T to predict the same P_{ent}. Entrapment pressures calculated from Raman measurements of quartz inclusions at elevated T (P_{ent}^{464}) use P_{incl}^{464} determined from quartz at various temperatures during heating of the

289 sample, the T during heating measurements, and an assumed entrapment T (see Figure S1 for a
290 schematic illustration of the calculation method).

291 Molar volumes (V) of quartz were calculated using the quartz parameters of Angel et al.
292 (2017a), and following their curved boundary model approach. Thermodynamic properties of
293 epidote and clinozoisite were derived from the experimental P-T-V data of Gatta et al. (2011), and
294 Qin et al. 2016 Pawley et al. (1996), respectively. P-T-V data were fit using EoSFit7c (Angel et
295 al. 2014). Epidote and clinozoisite data were fit with the modified Tait Equation of State (EoS)
296 and thermal pressure term (Fig. S2). The clinozoisite thermodynamic properties are less well
297 constrained, because the P-T-V data are derived from two experimental sources that used different
298 epidote crystals (bulk modulus from Qin et al. 2016, $X_{ep} = 0.39$; thermal expansivity from Pawley
299 et al. 1996, $X_{ep} = 0.02$); therefore, the thermodynamic properties calculated using data from two
300 different sources may have a larger uncertainty. The clinozoisite P-V data of Qin et al. (2016) were
301 used because it shows smaller errors, and to the best of our knowledge, no updated T-V data exist
302 for clinozoisite. For zoisite, we use the reference bulk modulus and thermal expansivity given in
303 Holland and Powell (2011), and the Tait EoS and thermal pressure term (Table 2). Shear moduli
304 for epidote, clinozoisite, and zoisite were calculated by implementing the aggregate Poisson's ratio
305 of 0.26 from Mao et al. (2007) and the determined bulk moduli (Table 2). The shear modulus for
306 an isotropic material is given by:

307 $$G = \frac{3K(1-2\nu)}{2(1+\nu)}$$

308 where G is the shear modulus, K is the bulk modulus, and ν is the Poisson ratio. This relationship
309 predicts a shear modulus for epidote of 65.1 GPa, calculated from the Gatta et al. (2011) bulk
310 modulus (Table 2); the calculated value closely approximates experimentally determined values

311 (e.g., 61.2 GPa, Ryzhova et al. 1966). We are not aware of experimental shear modulus data for
312 clinozoisite; therefore, to maintain internal consistency we calculate shear moduli using our
313 regressed bulk moduli and equation 2; the calculated shear moduli are given in Table 2. The small
314 difference between experimentally-derived and calculated shear moduli have a minimal effect on
315 P_{ent}. The molar volume and shear modulus of epidote and clinozoisite solid-solution compositions
316 were calculated assuming ideal (linear) mixing. A comparison of epidote V-X_{ep} (mol fraction of
317 epidote) that is based on the compilation of Franz and Liebscher (2004) shows that linear mixing
318 of molar volumes is an appropriate approximation (Fig. S3). Elastic modeling suggests that X_{ep}
319 has a greater influence on calculated entrapment pressures when epidote preserves quartz with
320 higher P_{incl} (Fig. 1D).

321 **Results and Discussion**

322 **Raman analyses at ambient conditions**

323 We compare P_{incl}^{464} of samples HF14C and LdC-31C with P_{incl} calculated from hydrostatic
324 calibrations of Raman shifts of the 128 cm^{-1} (P_{incl}^{128}) and 206 cm^{-1} (P_{incl}^{206}) quartz bands with pressure
325 (Schmidt and Ziemann, 2000), and with strains ($P_{incl}^{strains}$). If we assume a $P_{incl}^{strains}$ error (1σ) that is
326 equal to the error of P_{incl}^{464}, P_{incl} calculated from both approaches are within error (1σ, Fig. 5, Tables
327 S2, S3). We note that the $P_{incl}^{strains}$ error is a minimum uncertainty, because the errors associated with
328 peak fitting for the quartz 128 cm^{-1} and 206 cm^{-1} bands are significant (Tables S2, S3).

329 P_{incl} estimates for sample HF14C resulting from hydrostatic calibrations of Raman shifts of
330 quartz 128, 206, and 464 cm^{-1} bands are statistically identical (within error, 1σ): P_{incl}^{128} = 29 ± 37
331 MPa, P_{incl}^{206} = 27 ± 23 MPa, and P_{incl}^{464} = 15 ± 26 MPa (1σ, Fig. 5, Table S2). $P_{incl}^{strains}$ (48 MPa) indicates
332 a slightly higher P_{incl} than that predicted from hydrostatic calibrations; however, the similar

inclusion pressures calculated from hydrostatic calibrations and strains suggest that this quartz inclusion retains nominal strain anisotropy. Quartz inclusions from sample LdC-31C retain residual pressures of: P_{incl}^{128} = 90 ± 31 MPa, P_{incl}^{206} = 125 ± 77 MPa, P_{incl}^{464} = 144 ± 23 MPa (inclusion 1, 1σ) and P_{incl}^{128} = 157 ± 32 MPa, P_{incl}^{206} = 140 ± 21 MPa, P_{incl}^{464} = 175 ± 24 MPa (inclusion 2, 1σ). $P_{incl}^{strains}$ for both inclusions are slightly higher than predicted by the hydrostatic calibrations: $P_{incl}^{strains}$ = 183 MPa (inclusion 1) and $P_{incl}^{strains}$ = 191 MPa (inclusion 2) (Fig. 5, Table S3). LdC-31C inclusion 1 seems to record the largest anisotropy, as shown by the difference in inclusion pressures from hydrostatic calibrations. However, P_{incl}^{464} is within error of $P_{incl}^{strains}$ for all inclusions in samples HF14C and LdC-31C. The difference in P_{incl} calculated from P_{incl}^{464} and from strains results in a difference of < 0.07 GPa in the final calculated entrapment pressure (Tables S2, S3).

We can further quantify the anisotropy of the α-quartz inclusions with trigonal symmetry ($\varepsilon_1 = \varepsilon_2$) by comparing strains that were determined from shifts of Raman band positions and the phonon-mode Grüneisen tensor, using the equation:

$$\Delta\varepsilon = \frac{\varepsilon_1 + \varepsilon_2}{2} - \varepsilon_3$$

The difference in strains (Δε) suggests that the HF14C quartz inclusion (Δε = -0.0017, Table S2) records anisotropy similar to LdC-31C inclusion 2 (inclusion 1: Δε = -0.0034, inclusion 2: Δε = -0.0013, Table S3). LdC-31C inclusion 1 records the largest anisotropy, but the limitations of using an isotropic elastic model and current EoS to predict the pressure evolution of this inclusion (P_{incl}^{mod}) showing greater anisotropy can only be evaluated up to 200 °C because the heating measurement was aborted when the window in the heating stage cracked (Fig. 4).

Raman analyses at elevated temperature

All quartz inclusions exhibited a shift of the 464 cm^{-1} band position to lower wavenumbers with increasing temperature, but encapsulated inclusions exhibit less of a shift compared to Raman bands of the Herkimer quartz standard analyzed at 0.1 MPa and the measurement temperature (Fig. 4). At elevated temperatures, we encountered difficulties in separating the quartz 464 cm^{-1} band and epidote shoulder bands due to their convergence that results from the T-dependence of Raman shifts and broadening of both the quartz and epidote bands with increasing temperature. The convergence of quartz and epidote bands caused a significant increase in peak fit errors, resulting in greater uncertainties associated with $\Delta\omega$, P^{464}_{incl}, and P^{464}_{ent} values at elevated T (Fig. 4, 6, 7). At all temperatures, P^{464}_{incl} calculated from Raman measurements during heating and cooling are within error (1σ) , and P^{464}_{incl} errors (1σ) exceed the difference between P^{mod}_{incl} (modeled) and P^{464}_{incl}; above 250 °C, peak fitting errors increase significantly (Fig. 6, 7B). The increase in peak fit uncertainty makes it challenging to determine with confidence if the elastic model and associated EoS reproduce P^{464}_{incl} at elevated temperatures.

Samples HF14C and LdC-31C displayed the largest increase in P^{464}_{incl} during heating. The P^{464}_{incl} for sample HF14C is sufficiently low such that the quartz inclusion approaches the α-β transition during heating to 600 °C, and hence records a large increase in P^{464}_{incl}. P^{464}_{incl} calculated from measurements at elevated temperatures underestimated P^{mod}_{incl} significantly at low to moderate temperatures; however, the general trend of P^{mod}_{incl} is matched by P^{464}_{incl} at high temperatures (Fig. 6). Sample LdC-31C retains quartz inclusions with a higher P^{464}_{incl} such that during heating the α-β transition temperature is significantly higher than 600°C and the trend is not influenced by the α-β transition. Nonetheless, quartz inclusion (# 2) records the largest increase in P^{464}_{incl} that also matches the trend of P^{mod}_{incl}. P^{464}_{incl} calculated from LdC-31C inclusion 1 is within error of P^{mod}_{incl} up to

the final measurement temperature at 200 °C. Sample FT1E exhibits the smallest increase in P_{incl}^{464} during heating, and P_{incl}^{464} calculated at super-ambient temperatures significantly underestimates P_{incl}^{mod} (Fig. 6). However, all P_{incl}^{464} values are within error (1σ) of P_{incl}^{mod}, owing to the high uncertainty associated with peak fits of sample FT1E. The lower P_{incl}^{464} values obtained during heating likely reflect an overestimation of P_{incl}^{mod} by the elastic model and associated EoS, quartz anisotropy, measurement and peak fitting errors, or some combination of all of these factors; therefore, we do not use data from this inclusion to assess the reliability of the elastic model and EoS. It is possible that the quartz inclusion from sample FT1E records more anisotropic strain, or that the least thermally expansive axis of quartz is oriented parallel to the *c*-axis of epidote (maximum thermal expansivity), and therefore records a nominal pressure increase. Nonetheless, based on P_{incl}^{464} calculated from the lower temperature measurements of samples HF14C, LdC-31C, and FT1E (≤ 250 °C), our results suggest that application of the current equations of state, with an isotropic elastic model, satisfactorily simulates the evolution of P_{incl} with increasing temperature for anisotropic minerals (quartz and epidote).

Evaluation of calculated entrapment pressures at elevated temperatures

To evaluate the applicability of the elastic model and EoS for estimating entrapment pressures of quartz inclusions in epidote, we calculate entrapment pressures (P_{ent}^{464}) from P_{incl}^{464} derived at elevated temperatures (Fig. 7). Low P_{incl}^{464} sample HF14C showed the largest variation in calculated entrapment pressures, and measurements result in lower entrapment pressures relative to theoretical estimates at low temperatures. However, large uncertainties are associated with peak fits from sample HF14C due to the overlap of the quartz 464 cm^{-1} band with epidote shoulder bands, making peak deconvolution less robust. Likewise, sample FT1E exhibited a general

decrease in P_{ent}^{464} with increasing T, but the quartz 464 cm^{-1} band exhibited a strong overlap with neighboring epidote bands at ambient and increasing T (Fig. 3F). Owing to these large uncertainties, it is challenging to use HF14C and FT1E data to evaluate whether entrapment pressure calculations require a thermal correction. We limit P_{ent}^{464} to T ≤ 250 °C, a temperature at which most errors in P_{incl}^{464} are < 0.1 GPa (Fig. 7A), to evaluate the need for a correction to P_{ent} calculated at elevated T. For these measurements, entrapment pressures calculated from P_{incl}^{464} of heated inclusions exhibit only small differences compared to entrapment pressures calculated from P_{ent}^{mod}. Most inclusions exhibit a decrease in absolute P_{ent}^{464} with increasing T, but all P_{ent}^{464} values remain within error (1σ) of modeled P_{ent}. We can also evaluate the difference between the mean P_{ent}^{464} of all Raman analyses of a single inclusion and P_{ent}^{mod}. We evaluate the weighted mean of Raman analyses of our analyzed inclusions by assigning a weight (ω_i) to each calculated P_{ent}^{464} that considers measurement uncertainty:

$$\omega_i = 1/\sigma_i^2$$

where σ_i is the 1σ error of each P_{ent}^{464} calculation (Tables S2, S3, S4). For samples HF14C, LdC-31C, and FT1E, we calculate P_{ent}^{464} weighted means of 0.41 GPa, 0.79 GPa and 0.86 GPa, and 1.67 GPa, respectively. These values slightly underestimate, but closely approximate, calculated P_{ent}^{mod} values of 0.49 GPa, 0.82 and 0.87 GPa, and 1.75 GPa, respectively. These observations suggest that the errors introduced by associated EoS, an isotropic elastic model, and Grüneisen tensor components are minimal, and that the calculated entrapment pressure is not a function of the temperature at which the sample is analyzed (Fig. 7).

Comparison of calculated entrapment pressures to previously reported P-T histories

To assess if the quartz-in-epidote barometer provides reasonable estimates of the pressure of epidote growth, we compare our results to previously determined P-T conditions for our samples.

Upper Schierferhuelle – Sample HF14C

Sample HF14C preserves foliation parallel epidotes that appear to have crystallized pre-or-syn-kinematic to fabric-forming deformation (Fig. 2A). Development of the dominant foliation (S1) observed in the mafic sample is proposed to have occurred early in the metamorphic history of the USH. This foliation was overprinted by static lawsonite growth in the mafic samples, and at least some of the epidote is associated with subsequent breakdown of lawsonite. A subsequent shear foliation subparallel to S1 is evident in the pelites, but not in the mafic rocks at the sample localities (Selverstone 1985). Garnet growth in pelites occurred after lawsonite breakdown, and rotated garnets indicate that they formed during development of the subparallel shear foliation (S1, Selverstone 1985). Epidote inclusions are found within garnets that formed near peak T. It is thus likely that matrix epidote analyzed in the mafic sample formed early, before USH rocks reach peak T. The epidote analyzed from this sample encapsulates a quartz inclusion with a residual $P_{incl}^{464} = 15 \pm 26$ (1σ) MPa, or $P_{incl}^{strains} = 48$ MPa. Assuming an entrapment temperature of 475 ºC (below peak T of ~ 500 °C), we estimate entrapment pressures of 0.49 ± 0.10 (2σ) GPa from P_{incl}^{464}, and 0.55 GPa from $P_{incl}^{strains}$ (Fig. 7A, Table S2). These P-T estimates likely reflect epidote growth conditions prior to reaching peak T conditions, and our results are consistent with petrographic observations and previously established P-T constraints; these previous P-T constraints are derived from a range of thermobarometry approaches that give consistent results related to the P-T evolution of these samples (cation thermobarometry, Gibbs garnet modeling, and fluid inclusion thermobarometry; Selverstone and Spear 1985). It is possible that overstepping of reaction boundaries occurred

during formation of epidotes, but the agreement of our results with petrographic constraints and independent thermobarometry suggest that overstepping did not significantly affect the P-T estimates obtained here.

Lago di Cignana – Sample LdC-31C

Quartz inclusions 1 and 2 from sample LdC-31C retain residual pressures of P_{incl}^{464} = 143 ± 23 (1σ) MPa and P_{incl}^{464} = 175 ± 24 (1σ) MPa, or $P_{incl}^{strains}$ = 183 MPa and $P_{incl}^{strains}$ = 191 MPa, respectively. Assuming an entrapment temperature of 550 ºC, we calculate an entrapment pressure of ~0.8-0.9 ± 0.08 (2σ) GPa (Fig. 7A, Table S3). This estimate is much lower than the reported peak metamorphic conditions of ~600 ºC and 3.2 – 3.4 GPa (within the diamond-bearing horizon at Lago di Cignana; Frezzotti et al. 2011). However, the presence of quartz inclusions in epidote is clear evidence that the qtz-in-ep entrapment pressures do not record peak pressure conditions, where coesite is stable. Our calculated entrapment pressures, and field and petrographic relationships of epidote-fuchsite veins encased in the high-P foliation, suggests that epidote growth represents an early vein formation stage that predates HP/LT metamorphism in the Lago Di Cignana region or, alternatively, that the late epidote vein formed during exhumation and experienced only minor deformation (Fig. 2B). Our P-T estimates for sample LdC-31C are also consistent with retrograde metamorphic conditions that have been suggested by van der Klauw et al. (1997) (T = 550 - 500 ºC, P ≈ 1.8 GPa; T = 350 – 450 ºC, P ≈ 0.35 – 0.55 GPa); however, our samples show no evidence for extensive retrogression as represented by the preservation of HP assemblages. It is most likely that the epidote vein formed during exhumation and after leaving the coesite-stable field. If the epidote veins formed along the prograde path and before reaching peak conditions, the epidotes would have encapsulated quartz and would traverse through the coesite-stable field at peak conditions and then return to the quartz-stable region during

exhumation. The preservation of quartz inclusions in these epidotes would require kinetic barriers to prevent formation of coesite at peak conditions or, conversely, mass conversion of coesite back to quartz along the retrograde path. While this scenario is possible, it is more likely that the epidote formed late, during exhumation and while P-T conditions were in the quartz stable field.

Frosnitz Tal – Sample FT1E

Epidotes in sample FT1E are aligned parallel to the primary foliation, suggesting pre-to syn-tectonic crystallization of epidote (Fig. 2C). The quartz inclusion analyzed from sample FT1E retains a residual inclusion pressure of P_{incl}^{464} = 573 ± 30 (1σ) MPa. Assuming an entrapment temperature of 625 ºC, our results suggest a formation pressure of 1.75 ± 0.12 (2σ) GPa (Fig. 7A). Our predicted pressure is slightly lower than previous peak P-T estimates for the Frosnitz Tal eclogite zone in the Tauern Window (T ≈ 600 ºC, P ≈ 1.9 – 2.5 GPa) (e.g., Spear and Franz 1986; Selverstone et al. 1992). Epidote growth conditions are further constrained by petrographic observations. Banded eclogites from the Frosnitz Tal contain epidote-zoisite pairs in apparent textural equilibrium, suggesting a transformation loop at ~ 2.0 GPa, 625 °C (Selverstone et al. 1992). Pseudosection models of banded eclogites from Eissee (Tauern Window eclogite zone) predict growth of matrix zoisite during exhumation at P-T conditions below ~ 1.9 GPa and ~625 °C (Hoschek 2007); however, pseudosections based on samples that have different bulk rock compositions should be compared with caution.

Corrections to the thermal component of the elastic model

The agreement between P_{incl}^{464} (measured) and P_{incl}^{mod} (P_{incl} predicted by elastic modeling) at T ≤ 250 °C tentatively suggests that entrapment pressures calculated from the quartz-in-epidote barometer do not require a temperature-dependent correction; i.e., an empirical correction to

entrapment pressures (based on the estimated entrapment temperature) that accounts for elastic modeling or EoS errors, is not required. We note that at T > 250 °C, it is more difficult to evaluate the current elastic modeling approach and associated EoS, and our interpretation is limited by errors associated with fitting of the quartz 464 cm^{-1} band at elevated T. Our interpretation is consistent with results from the apatite-in-garnet barometer that conclude that a temperature correction is not needed for apatite inclusion pressure measurements conducted at ambient temperature and that are subsequently used to calculate entrapment pressures at higher temperatures (Ashley et al. 2017). In comparison, previous work suggests that a temperature correction is required for the qtz-in-grt barometer when the Raman 464 cm^{-1} band is used for inclusion P determination (Ashley et al. 2016). These somewhat contradictory results (i.e., no observed offset in measured and modeled inclusion P at elevated temperatures) are problematic, given that quartz is the common inclusion phase between the qtz-in-grt and qtz-in-ep barometers. P_{incl} estimates based on different quartz inclusion bands and strains are similar in this study and hence, the P_{incl}^{464} and P_{incl}^{mod} are similar, but significant disparities in pressures obtained from the different bands are observed for quartz in garnet, suggesting significant anisotropy (Bonazzi et al. 2019). Perhaps the lower bulk modulus of epidote results in a smaller stress anisotropy for the quartz inclusion that is not detectable with current methods. Additionally, because quartz and epidote typically (re)crystallize along a schistosity during fabric development, it may be that the orientation of the quartz inclusion relative to the epidote host leads to a bulk stress tensor that optimally characterizes the inclusion P for the system, and in this case, the mutual orientation of quartz inclusions in epidote minimizes quartz anisotropy due to the anisotropic expansion of epidote during heating (Gatta et al. 2011). Furthermore, the quartz inclusion in sample FT1E may record the largest anisotropy and the deviation of absolute values of P_{ent}^{464} from modeled P_{ent} may

be real, but we cannot fully evaluate the extent of anisotropy preserved by this quartz inclusion. Regardless of the mechanism, our results lead to the following conclusions: 1) inclusion pressures calculated from the hydrostatic calibration of the quartz 464 cm^{-1} Raman band shifts (not valid for high anisotropic strain), yield nearly constant entrapment pressures (within uncertainty), independent of the temperature at which the inclusion is analyzed; and 2) allowing for errors introduced by modeling of entrapment pressures, our results suggest that the 1D-isotropic model is appropriate for modeling the elastic behavior of these two anisotropic phases, and no further correction is required for calculation of final entrapment pressures.

Quartz-in-epidote barometry limitations

A major limitation of the quartz-in-epidote barometer is related to the convergence of the 464 cm^{-1} Raman band of quartz (and other quartz bands) and the epidote shoulder bands as temperature is increased, causing peak overlap and requiring deconvolution to fit the quartz band. However, robust peak fits can be applied to most standard Raman measurements made at ambient T, wherein the peak overlap is less significant because the separation between the quartz 464 cm^{-1} band and epidote shoulder bands is larger. Elastic thermobarometry requires robust determination of positions of multiple bands to calculate strains and to account for anisotropy (Murri et al. 2018, 2019; Angel et al. 2019); however, epidotes contain many bands that overlap with quartz bands, especially those near 128 cm^{-1}, 206 cm^{-1}, and 464 cm^{-1}. To minimize uncertainties associated with fitting quartz peaks, sufficiently high quartz inclusion Raman intensities may be achieved by rotating samples to analyze quartz inclusions in different orientations. Different epidote and quartz bands will reach maximum intensities at different orientations due to the orientation-dependent polarizability of mineral vibrational modes (Raman band positions will not change), but an orientation that makes the quartz Raman bands dominant can minimize peak fitting uncertainties.

Additionally, the Raman spectra of epidotes may be subtracted from the convolved Raman spectra of quartz and epidote to obtain a pure quartz Raman spectrum, but this would require careful evaluation. Choosing samples from high-P rocks that preserve quartz with high residual P_{incl}, may also limit overlap of quartz bands (e.g., 464 cm^{-1}) with high intensity epidote bands near ~ 425 cm^{-1} and 455 cm^{-1}. For high-T/low-P samples, convergence of the 464 cm^{-1} quartz band may not allow separation of the quartz and epidote bands via deconvolution, perhaps limiting application of qtz-in-ep barometry to epidote crystals that have entrapped quartz under moderate to high pressure conditions. Further analyses using epidotes from magmatic systems or skarns that have well constrained P-T histories might help better understand the limitations of the technique.

We emphasize that our approach does not allow us to fully evaluate the reliability of the calculated entrapment pressures because we cannot demonstrate that reactions that produce epidote were not significantly overstepped. The importance of overstepping will depend on the relationship of the qtz-in-ep isomekes and the slope (dP/dT) of the epidote-in reaction line. Because qtz-in-ep isomekes are nearly flat, if the epidote-in reaction line is flat (dP/dT = 0) or vertical (dT/dP = 0), the effect of T is minimal. Between these extremes overstepping may become important, and will depend on the relative slopes of the qtz-in-ep isomekes and reaction line, and the P-T path of the rock. Furthermore, we cannot unambiguously determine if the final P_{ent}^{464} of sample FT1E is affected by quartz anisotropy; therefore, we advise that the uncertainties that we report for the entrapment pressures below be applied with caution. In spite of these concerns, the relatively good correlation between pressure determined here and P-T estimates and petrographic, field, and petrologic studies of the same areas provides confidence that the qtz-in-ep barometer provides reasonable pressure estimates in some cases. Future recommended studies would include comparing qtz-in-ep pressure estimates with additional samples that have good field, petrographic,

556 and independent thermobarometry constraints, with modeled reactions that include both epidote
557 and quartz as product phases, and/or synthesis experiments of quartz inclusions in epidote (e.g.,
558 Thomas and Spear, 2018; Bonazzi et al., 2019).

559 **Final comments and implications**

560 This work highlights the potential of the qtz-in-ep barometer to constrain formation
561 conditions of epidote, and also highlights some of the obstacles and uncertainties associated with
562 implementing this barometer. The qtz-in-ep barometer was evaluated for moderate to high-P
563 metamorphic rocks, but can potentially be applied to understand formation conditions of other
564 geologic processes that include epidote-bearing skarn formation, epidote growth in ore deposits,
565 epidote-bearing granitoid rocks, hydrothermal alteration of oceanic crust, and growth conditions
566 of epidote in metamorphic rocks from convergent margins. Although entrapment pressures
567 calculated from the qtz-in-ep barometer are in general consistent with previous estimates for the
568 samples studied, further work is needed to document the accuracy and reliability of entrapment
569 pressures (e.g., synthesis experiments, or detailed petrographic studies that integrate reaction
570 modeling). Nevertheless, qtz-in-ep entrapment pressures of samples from the Frosnitz Tal eclogite
571 zone in the Tauern Window and the Upper Schieferhuelle in the Western Tauern are in general
572 agreement with previously-established P-T conditions. Qtz-in-ep entrapment pressures of samples
573 from Lago di Cignana indicate vein epidote crystallization below maximum pressure conditions
574 of the area (diamond stability field). The presence of quartz inclusions suggests that the qtz-in-ep
575 barometer records P-T conditions that are not in the diamond stability field, due to the lack of
576 coesite, and highlights how field and petrographic observations can be combined with the
577 barometer to better constrain cryptic stages of P-T histories. Furthermore, results of our analyses
578 at various temperatures suggest that a temperature-dependent entrapment pressure correction is

579 not required, contrary to what has been noted for the qtz-in-grt barometer. Therefore, this work
580 suggests that Raman measurements of quartz inclusions in epidote taken at ambient conditions can
581 be used to calculate high-temperature entrapment pressures without applying temperature
582 corrections (for quartz inclusions preserving near isotropic strains). Our results further highlight
583 the importance of integrating data from mineral geobarometers with field and petrographic
584 observations that document the relative timing of various mineral formation and deformation
585 events to constraint P-T conditions associated with development of distinct structural and textural
586 fabrics.

587 **Acknowledgements**

588 The authors thank J. Selverstone for providing the reference samples used in this study and
589 for informal reviews, M. Alvaro and R. Angel for help with evaluating P-T-V data, M. Murri and
590 N. Campomenosi for discussions about Raman data reduction, and M. Mazzuchelli and M Gilio
591 for helpful manuscript comments. We thank C. Cannatelli and D. Baker for editorial handling, and
592 F. Spear and an anonymous reviewer for constructive reviews that greatly improved this
593 manuscript. We thank T. Holland for assistance with modeling quartz volumes and Charles Farley
594 for assistance with use of the Raman Microprobe at Virginia Tech. This work was supported by a
595 Geological Society of America Student Research Grant and a Ford Foundation Fellowship
596 awarded to M.C., and National Science Foundation Grants (EAR-1725110) awarded to J. Barnes,
597 W. Behr, and D. Stockli, and to R.B. (EAR-479533).

598 **Figure Captions**

599 **Figure 1.** (a) Schematic illustration of the evolution of a host phase (e.g., epidote) and an inclusion
600 (e.g., quartz) during exhumation, and the residual pressure (P_{incl}) retained by a quartz inclusion at
601 ambient T (modified from Guiraud and Powell 2006; Befus et al. 2018). Models of the P-T
602 dependence of P_{incl} for quartz in (b) epidote, (c) clinozoisite, and (d) zoisite. Models vary over the
603 range of P_{incl} = -0.2 GPa to 0.8 GPa (0.1 GPa intervals) and from 400 ºC – 800 ºC. Models show
604 that P_{incl} is nominally affected by the assumed entrapment temperature. Dependence of entrapment
605 pressure (e) and temperature (f) on the mol fraction (X_{ep}) of Al-Fe monoclinic epidote at T = 500
606 °C and P = 1 GPa, respectively. At low P_{incl}, the composition of epidote minimally affects the final
607 entrapment pressure or temperature. At higher P_{incl}, the final entrapment pressure and temperature
608 are more dependent on X_{ep}. Regions in grey denote conditions at which P_{incl} is below 0 GPa,
609 wherein quartz preserves a tensile stress.

610 **Figure 2.** Photomicrographs of thin sections showing the petrographic relationships of epidotes
611 analyzed in this study. (a) HF14C: foliation parallel epidote grains suggest that epidote likely grew
612 prior to or during deformation associated with formation of the primary foliation. (b) LdC-31C:
613 analyzed epidotes are from a vein that has an irregular, undulating contact with the primary
614 foliation. The petrographic relations suggest that epidote crystallized prior to formation of the
615 HP/LT foliation, or during exhumation. This fabric and the presence of quartz inclusions and lack
616 of coesite suggests that the epidotes record formation pressures below high-pressure conditions
617 where coesite is stable. (c) FT1E: epidote grains aligned parallel to foliation, suggesting that
618 crystallization occurred prior to, or during, the formation of the primary foliation.

619 **Figure 3.** Raman spectra of epidotes (a) R060284 (X_{ep} = 0.30) and (b) R050131 (X_{ep} = 0.76) from
620 the RRUFF database, and Raman spectra of all samples at ambient conditions and their associated

peaks after fitting. (a, b) Raman spectra of epidotes are shown in two epidote orientations (red and blue lines) over the wavenumber region 380-540 cm^{-1}. (c, d, e, f) Shown in circles are the Raman spectra, the dashed blue line is the fit to the Raman spectra, and solid lines indicate the peaks used to fit the quartz 464 cm^{-1} band (red), epidote bands (grey), and the 520.3 cm^{-1} Ar-plasma line (blue).

Figure 4. Raman shifts of the quartz (inclusion) 464 cm^{-1} band for the three samples measured during heating measurements. All samples display a decrease in wavenumber with increasing temperature. Relative to the position of the 464 cm^{-1} band of Herkimer quartz measured at ambient pressure, all inclusions exhibit a smaller change in the Raman shift of the quartz 464 cm^{-1} band due to an increase in inclusion pressure with increasing temperature. The solid black line is derived from the reference polynomial equation for the change in Raman shift of Herkimer quartz at 0.1 MPa and analysis T (Ashley et al. 2016). The dashed line is the linear extrapolation of the polynomial equation used to correct Raman shifts from samples LdC-31C and FT-1E relative to Herkimer quartz at measurement conditions. Error bars are propagated errors from instrument uncertainty, and errors associated with fitting quartz 464 cm^{-1} bands and the Ar plasma line. Symbols represent the following samples: FT1E (yellow diamond), LdC-31C inclusion 1 (grey circle), LdC-31C inclusion 2 (red circle) HF14C (blue square). White (open) symbols represent measurements made during cooling.

Figure 5. Comparison of P_{incl} calculated from the hydrostatic calibration of Raman shifts of quartz 128 cm^{-1}, 206 cm^{-1}, and 464 cm^{-1} bands, and P_{incl} calculated from strains. Yellow circles, red squares, and blue diamonds are the $P_{incl}^{strains}$ vs. P_{incl}^{464}, P_{incl}^{206} vs. P_{incl}^{464}, and P_{incl}^{128} vs. P_{incl}^{464} values, respectively. P_{incl} for sample LdC-31C (inclusion 2) is calculated at 23.7 °C and 23.8 °C. The

dashed line shows where P_{incl} calculated from different bands and strains would have the same values (1:1 line).

Figure 6. Inclusion pressures (P_{incl}^{464}) calculated from Raman analyses conducted during heating (symbols), compared to the P_{incl} evolution predicted by elastic modeling (P_{incl}^{mod}). The dashed lines represent P_{incl}^{mod}. P_{incl}^{464} errors (1σ) show the increase in error with increasing temperature. The error exceeds the difference between P_{incl}^{464} and P_{incl}^{mod}. Symbols represent the following samples: FT1E (yellow diamond), LdC-31C inclusion 1 (grey circle), LdC-31C inclusion 2 (red circle) HF14C (blue square). White (open) symbols are the measurements made during cooling.

Figure 7. (a) Entrapment pressures calculated from P_{incl}^{464} determined from Raman shifts of quartz inclusions during heating (relative to a quartz crystal at 0.1 MPa and measurement T), and comparison with model estimates of the temperature-dependence of entrapment pressure (solid lines). Transparent colored lines bound errors of entrapment pressure estimates (± 2σ). (b) Reference P-T conditions for samples FT1E and HF14C (grey boxes) and our estimated qtz-in-ep barometry entrapment pressures are shown for comparison. See text for discussion of the reference P-T conditions. Symbols represent the following samples: FT1E (yellow diamond), LdC-31C inclusion 1 (grey circle), LdC-31C inclusion 2 (red circle) HF14C (blue square). White (open) symbols represent measurements made during cooling.

References

Angel, R.J., Alvaro, M., and Gonzalez-Platas, J. (2014) EosFit7c and a Fortran module (library) for equation of state calculations. Zeitschrift für Kristallographie - Crystalline Materials, 229, 405–419.

Angel, R.J., Alvaro, M., Miletich, R., and Nestola, F. (2017a) A simple and generalised P–T–V EoS for continuous phase transitions, implemented in EosFit and applied to quartz. Contributions to Mineralogy and Petrology, 172, 29.

Angel, R.J., Mazzucchelli, M.L., Alvaro, M., and Nestola, F. (2017b) EosFit-Pinc: A simple GUI for host-inclusion elastic thermobarometry. American Mineralogist, 102, 1957–1960.

Angel, R.J., Murri, M., Mihailova, B., and Alvaro, M. (2019) Stress, strain and Raman shifts. Zeitschrift für Kristallographie - Crystalline Materials, 234, 129–140.

Anzolini, C., Nestola, F., Mazzucchelli, M.L., Alvaro, M., Nimis, P., Gianese, A., Morganti, S., Marone, F., Campione, M., Hutchison, M.T., and others (2019) Depth of diamond formation obtained from single periclase inclusions. Geology, 47, 219–222.

Ashley, K.T., Caddick, M.J., Steele-MacInnis, M.J., Bodnar, R.J., and Dragovic, B. (2014) Geothermobarometric history of subduction recorded by quartz inclusions in garnet. Geochemistry, Geophysics, Geosystems, 15, 350–360.

Ashley, K.T., Darling, R.S., Bodnar, R.J., and Law, R.D. (2015) Significance of "stretched" mineral inclusions for reconstructing P–T exhumation history. Contributions to Mineralogy and Petrology, 169, 55.

Ashley, K.T., Steele-MacInnis, M., Bodnar, R.J., and Darling, R.S. (2016) Quartz-in-garnet inclusion barometry under fire: Reducing uncertainty from model estimates. Geology, 44, 699–702.

Ashley, K.T., Barkoff, D.W., and Steele-MacInnis, M. (2017) Barometric constraints based on apatite inclusions in garnet. American Mineralogist, 102, 743–749.

Barkoff, D.W., Ashley, K.T., and Steele-MacInnis, M. (2017) Pressures of skarn mineralization at Casting Copper, Nevada, USA, based on apatite inclusions in garnet. Geology, 45, 947–950.

Barkoff, D.W., Ashley, K.T., Silva, R.G.D., Mazdab, F.K., and Steele-MacInnis, M. (2019) Thermobarometry of Three Skarns in the Ludwig Area, Nevada, Based On Raman Spectroscopy and Elastic Modeling of Mineral Inclusions in Garnet. The Canadian Mineralogist, 57, 25–45.

Befus, K.S., Lin, J.-F., Cisneros, M., and Fu, S. (2018) Feldspar Raman shift and application as a magmatic thermobarometer. American Mineralogist, 103, 600–609.

698 Behr, W.M., Kotowski, A.J., and Ashley, K.T. (2018) Dehydration-induced rheological
699 heterogeneity and the deep tremor source in warm subduction zones. Geology, 46, 475–
700 478.

701 Bonazzi, M., Tumiati, S., Thomas, J., Angel, R.J., and Alvaro, M. (2019) Assessment of the
702 reliability of elastic geobarometry with quartz inclusions. Lithos, 105201.

703 Campomenosi, N., Mazzucchelli, M.L., Mihailova, B., Scambelluri, M., Angel, R.J., Nestola, F.,
704 Reali, A., and Alvaro, M. (2018) How geometry and anisotropy affect residual strain in
705 host-inclusion systems: Coupling experimental and numerical approaches. American
706 Mineralogist, 103, 2032–2035.

707 Carlson, W.D. (2002) Scales of disequilibrium and rates of equilibration during metamorphism.
708 American Mineralogist, 87, 185–204.

709 Enami, M., Nishiyama, T., and Mouri, T. (2007) Laser Raman microspectrometry of
710 metamorphic quartz: A simple method for comparison of metamorphic pressures.
711 American Mineralogist, 92, 1303–1315.

712 Ferry, J.M., and Spear, F.S. (1978) Experimental calibration of the partitioning of Fe and Mg
713 between biotite and garnet. Contributions to Mineralogy and Petrology, 66, 113–117.

714 Franz, G., and Liebscher, A. (2004) Physical and Chemical Properties of the Epidote Minerals–
715 An Introduction–. Reviews in Mineralogy and Geochemistry, 56, 1–81.

716 Frezzotti, M.L., Selverstone, J., Sharp, Z.D., and Compagnoni, R. (2011) Carbonate dissolution
717 during subduction revealed by diamond-bearing rocks from the Alps. Nature Geoscience,
718 4, 703–706.

719 Gatta, G.D., Merlini, M., Lee, Y., and Poli, S. (2011) Behavior of epidote at high pressure and
720 high temperature: a powder diffraction study up to 10 GPa and 1,200 K. Physics and
721 Chemistry of Minerals, 38, 419–428.

722 Graves, P., and Gardiner, D. (1989) Practical raman spectroscopy. Springer.

723 Groppo, C., Beltrando, M., and Compagnoni, R. (2009) The P–T path of the ultra-high pressure
724 Lago Di Cignana and adjoining high-pressure meta-ophiolitic units: insights into the
725 evolution of the subducting Tethyan slab. Journal of Metamorphic Geology, 27, 207–231.

726 Guiraud, M., and Powell, R. (2006) P–V–T relationships and mineral equilibria in inclusions in
727 minerals. Earth and Planetary Science Letters, 244, 683–694.

728 Holland, T.J.B. (1979) High Water Activities in the Generation of High Pressure Kyanite
729 Eclogites of the Tauern Window, Austria. The Journal of Geology, 87, 1–27.

730 Holland, T.J.B., Redfern, S.A.T., and Pawley, A.R. (1996) Volume behavior of hydrous minerals
731 at high pressure and temperature: II. Compressibilities of lawsonite, zoisite, clinozoisite,
732 and epidote. American Mineralogist, 81, 341–348.

Hoschek, G. (2001) Thermobarometry of metasediments and metabasites from the Eclogite zone of the Hohe Tauern, Eastern Alps, Austria. Lithos, 59, 127–150.

——— (2007) Metamorphic peak conditions of eclogites in the Tauern Window, Eastern Alps, Austria: Thermobarometry of the assemblage garnet+omphacite+phengite+kyanite+quartz. Lithos, 93, 1–16.

Howell, D., Wood, I.G., Nestola, F., Nimis, P., and Nasdala, L. (2012) Inclusions under remnant pressure in diamond: a multi-technique approach. European Journal of Mineralogy, 24, 563–573.

Izraeli, E.S., Harris, J.W., and Navon, O. (1999) Raman barometry of diamond formation. Earth and Planetary Science Letters, 173, 351–360.

Kouketsu, Y., Enami, M., Mouri, T., Okamura, M., and Sakurai, T. (2014) Composite metamorphic history recorded in garnet porphyroblasts of Sambagawa metasediments in the Besshi region, central Shikoku, Southwest Japan. Island Arc, 23, 263–280.

Kueter, N., Soesilo, J., Fedortchouk, Y., Nestola, F., Belluco, L., Troch, J., Wälle, M., Guillong, M., Von Quadt, A., and Driesner, T. (2016) Tracing the depositional history of Kalimantan diamonds by zircon provenance and diamond morphology studies. Lithos, 265, 159–176.

Kurz, W., Neubauer, F., and Dachs, E. (1998) Eclogite meso- and microfabrics: implications for the burial and exhumation history of eclogites in the Tauern Window (Eastern Alps) from P-T-d paths. Tectonophysics, 285, 183–209.

Kuzmany, H. (2009) Solid-state spectroscopy: an introduction. Springer Science & Business Media.

Lafuente, B., Downs, R.T., Yang, H., and Stone, N. (2016) The power of databases: the RRUFF project. In Highlights in mineralogical crystallography pp. 1–29. Walter de Gruyter GmbH.

Mao, Z., Jiang, F., and Duffy, T.S. (2007) Single-crystal elasticity of zoisite Ca2Al3Si3O12 (OH) by Brillouin scattering. American Mineralogist, 92, 570–576.

Mazzucchelli, M.L., Burnley, P., Angel, R.J., Morganti, S., Domeneghetti, M.C., Nestola, F., and Alvaro, M. (2018) Elastic geothermobarometry: Corrections for the geometry of the host-inclusion system. Geology, 46, 231–234.

Miller, C., and Konzett, J. (2003) Magnesiochloritoid-talc-garnet assemblages from the Tauern Window, Eastern Alps, Austria: high pressure metamorphosed oceanic hydrothermal veins p. 5206. Presented at the EGS - AGU - EUG Joint Assembly.

Murri, M., Mazzucchelli, M.L., Campomenosi, N., Korsakov, A.V., Prencipe, M., Mihailova, B.D., Scambelluri, M., Angel, R.J., and Alvaro, M. (2018) Raman elastic geobarometry for anisotropic mineral inclusions. American Mineralogist, 103, 1869–1872.

769 Murri, M., Alvaro, M., Angel, R.J., Prencipe, M., and Mihailova, B.D. (2019) The effects of
770 non-hydrostatic stress on the structure and properties of alpha-quartz. Physics and
771 Chemistry of Minerals.

772 Nestola, F., Nimis, P., Ziberna, L., Longo, M., Marzoli, A., Harris, J.W., Manghnani, M.H., and
773 Fedortchouk, Y. (2011) First crystal-structure determination of olivine in diamond:
774 Composition and implications for provenance in the Earth's mantle. Earth and Planetary
775 Science Letters, 305, 249–255.

776 Nestola, F., Prencipe, M., Nimis, P., Sgreva, N., Perritt, S.H., Chinn, I.L., and Zaffiro, G. (2018)
777 Toward a Robust Elastic Geobarometry of Kyanite Inclusions in Eclogitic Diamonds.
778 Journal of Geophysical Research: Solid Earth.

779 Nestola, F., Zaffiro, G., Mazzucchelli, M.L., Nimis, P., Andreozzi, G.B., Periotto, B.,
780 Princivalle, F., Lenaz, D., Secco, L., Pasqualetto, L., and others (2019) Diamond-
781 inclusion system recording old deep lithosphere conditions at Udachnaya (Siberia).
782 Scientific Reports, 9, 1–8.

783 Nye, J.F. (1985) Physical properties of crystals: their representation by tensors and matrices.
784 Oxford university press.

785 Parkinson, C.D., and Katayama, I. (1999) Present-day ultrahigh-pressure conditions of coesite
786 inclusions in zircon and garnet: Evidence from laser Raman microspectroscopy. Geology,
787 27, 979–982.

788 Pawley, A.R., Redfern, S.A.T., and Holland, T.J.B. (1996) Volume behavior of hydrous minerals
789 at high pressure and temperature: I. Thermal expansion of lawsonite, zoisite, clinozoisite,
790 and diaspore. American Mineralogist, 81, 335–340.

791 Peacock, S.M. (1993) The importance of blueschist → eclogite dehydration reactions in
792 subducting oceanic crust. GSA Bulletin, 105, 684–694.

793 Qin, F., Wu, X., Wang, Y., Fan, D., Qin, S., Yang, K., Townsend, J.P., and Jacobsen, S.D.
794 (2016) High-pressure behavior of natural single-crystal epidote and clinozoisite up to 40
795 GPa. Physics and Chemistry of Minerals, 1–11.

796 Rubie, D.C. (1998) Disequilibrium during metamorphism: the role of nucleation kinetics.
797 Geological Society, London, Special Publications, 138, 199–214.

798 Ryzhova, T.V., Aleksandrov, K.S., and Korobkova, V.M. (1966) The elastic properties of rock-
799 forming minerals; V, Additional data on silicates. Physics of the Solid Earth, 2, 63–65.

800 Schmidt, C., and Ziemann, M.A. (2000) In-situ Raman spectroscopy of quartz: A pressure sensor
801 for hydrothermal diamond-anvil cell experiments at elevated temperatures. American
802 Mineralogist, 85, 1725–1734.

803 Selverstone, J. (1985) Petrologic constraints on imbrication, metamorphism, and uplift in the SW
804 Tauern Window, eastern Alps. Tectonics, 4, 687–704.

Selverstone, J., and Sharp, Z.D. (2013) Chlorine isotope constraints on fluid-rock interactions during subduction and exhumation of the Zermatt-Saas ophiolite. Geochemistry, Geophysics, Geosystems, 14, 4370–4391.

Selverstone, J., and Spear, F.S. (1985) Metamorphic P–T Paths from pelitic schists and greenstones from the south-west Tauern Window, Eastern Alps. Journal of Metamorphic Geology, 3, 439–465.

Selverstone, J., Franz, G., Thomas, S., and Getty, S. (1992) Fluid variability in 2 GPa eclogites as an indicator of fluid behavior during subduction. Contributions to Mineralogy and Petrology, 112, 341–357.

Sobolev, N.V., Fursenko, B.A., Goryainov, S.V., Shu, J., Hemley, R.J., Mao, H., and Boyd, F.R. (2000) Fossilized high pressure from the Earth's deep interior: The coesite-in-diamond barometer. Proceedings of the National Academy of Sciences, 97, 11875–11879.

Spear, F.S., and Franz, G. (1986) P-T evolution of metasediments from the Eclogite Zone, south-central Tauern Window, Austria. Lithos, 19, 219–234.

Spear, F.S., and Selverstone, J. (1983) Quantitative P-T paths from zoned minerals: Theory and tectonic applications. Contributions to Mineralogy and Petrology, 83, 348–357.

Spear, F.S., Thomas, J.B., and Hallett, B.W. (2014) Overstepping the garnet isograd: a comparison of QuiG barometry and thermodynamic modeling. Contributions to Mineralogy and Petrology, 168, 1059.

Thomas, J.B., and Spear, F.S. (2018) Experimental study of quartz inclusions in garnet at pressures up to 3.0 GPa: evaluating validity of the quartz-in-garnet inclusion elastic thermobarometer. Contributions to Mineralogy and Petrology, 173, 42.

Turner, F.J. (1981) Metamorphic petrology: Mineralogical, field, and tectonic aspects. Hemisphere Publishing Corporation.

van der Klauw, S.N.G.C., Reinecke, T., and Stöckhert, B. (1997) Exhumation of ultrahigh-pressure metamorphic oceanic crust from Lago di Cignana, Piemontese zone, western Alps: the structural record in metabasites. Lithos, 41, 79–102.

Wang, J., Mao, Z., Jiang, F., and Duffy, T.S. (2015) Elasticity of single-crystal quartz to 10 GPa. Physics and Chemistry of Minerals, 42, 203–212.

Zhong, X., Andersen, N.H., Dabrowski, M., and Jamtveit, B. (2019) Zircon and quartz inclusions in garnet used for complementary Raman thermobarometry: application to the Holsnøy eclogite, Bergen Arcs, Western Norway. Contributions to Mineralogy and Petrology, 174, 50.

This is a preprint, the final version is subject to change, of the American Mineralogist (MSA)
Cite as Authors (Year) Title. American Mineralogist, in press.
DOI: https://doi.org/10.2138/am-2020-7379

Table 1. Abbreviations used in this manuscript

Abbreviation	Definition
ω^{464}_{std}	Wavenumber position of the quartz 464 cm^{-1} band of a standard at a measurement T
ω^{464}_{incl}	Wavenumber position of the quartz 464 cm^{-1} band of an inclusion at a measurement T
$\Delta\omega^{464}_{shift}$	$\Delta\omega^{464}_{shift} = \omega^{464}_{incl} - \omega^{464}_{std}$
P^{128}_{incl}	Inclusion pressure calculated from the hydrostatic calibration of the quartz 128 cm^{-1} band
P^{206}_{incl}	Inclusion pressure calculated from the hydrostatic calibration of the quartz 206 cm^{-1} band
P^{464}_{incl}	Inclusion pressure calculated from the hydrostatic calibration of the quartz 464 cm^{-1} band
$P^{strains}_{incl}$	Inclusion pressure calculated from strains
P^{mod}_{incl}	Inclusion pressure predicted by elastic modeling (Fig. S1B)
P^{464}_{ent}	Entrapment pressure calculated from P^{464}_{incl}
HF14C	Sample from Upper Schieferhuelle
LdC-31C	Samples from Lago di Cignana
FT1E	Sample from Frosnitz Tal

This is a preprint, the final version is subject to change, of the American Mineralogist (MSA)
Cite as Authors (Year) Title. American Mineralogist, in press.
DOI: https://doi.org/10.2138/am-2020-7379

Table 2. Thermodynamic and Physical Properties of Clinozoisite, Epidote, and Zoisite

Phase	V_0 (cm^3 mol^{-1})	α_0 (10^5 K^{-1})	κ_0 (GPa)	κ_0'	κ_0'' $\kappa_0'' = -\kappa_0'/\kappa_0$	S_0 (J mol^{-1} K^{-1})	θ_E K
Clinozoisite	138.1(4)‡	2.24(6)*	147(2)‡	4.0‡	-0.0027	301▪	528.58
Epidote	138.06(9)†	2.25(3)†	115(2)†	6.7(5)†	-0.0058	315▪	512.38
Zoisite	135.80**	3.12**	104.4**	4.00**	-0.0038	298▪	532.19

All thermodynamic properties are given at standard state: 0.1 MPa, 298 K.

Einstein temperature (θ_E) is calculated from $\theta_E = 10636/(S_0/n_i + 6.44)$, where n_i is the number of ato

Reference P-V-T data from which thermodynamic properties are calculated:

‡Qin et. al, 2016 ($X_{Ep} = 0.39$), data fit with the Tait 2nd-order EoS.

*Pawley et. al, 1996 ($X_{Ep} = 0.02$), data fit with the Tait 2nd-order EoS and thermal pressure.

†Gatta et al., 2011 ($X_{Ep} = 0.74$), data fit with the Tait 3rd-order EoS and thermal pressure.

**Holland and Powell, 2011, Tait 2nd-order EoS and thermal pressure.

References from which thermodynamic and physical properties are derived:

▪Holland and Powell, 2011.

•Mao et al., 2007.

This is a preprint, the final version is subject to change, of the American Mineralogist (MSA)
Cite as Authors (Year) Title. American Mineralogist, in press.
DOI: https://doi.org/10.2138/am-2020-7379

ν (poisson ratio)	G (GPa)
0.26•	84.0
0.26•	65.7
0.26•	59.7

ms in epidote or zoisite (22).

This is a preprint, the final version is subject to change, of the American Mineralogist (MSA)
Cite as Authors (Year) Title. American Mineralogist, in press.
DOI: https://doi.org/10.2138/am-2020-7379

Figure 1

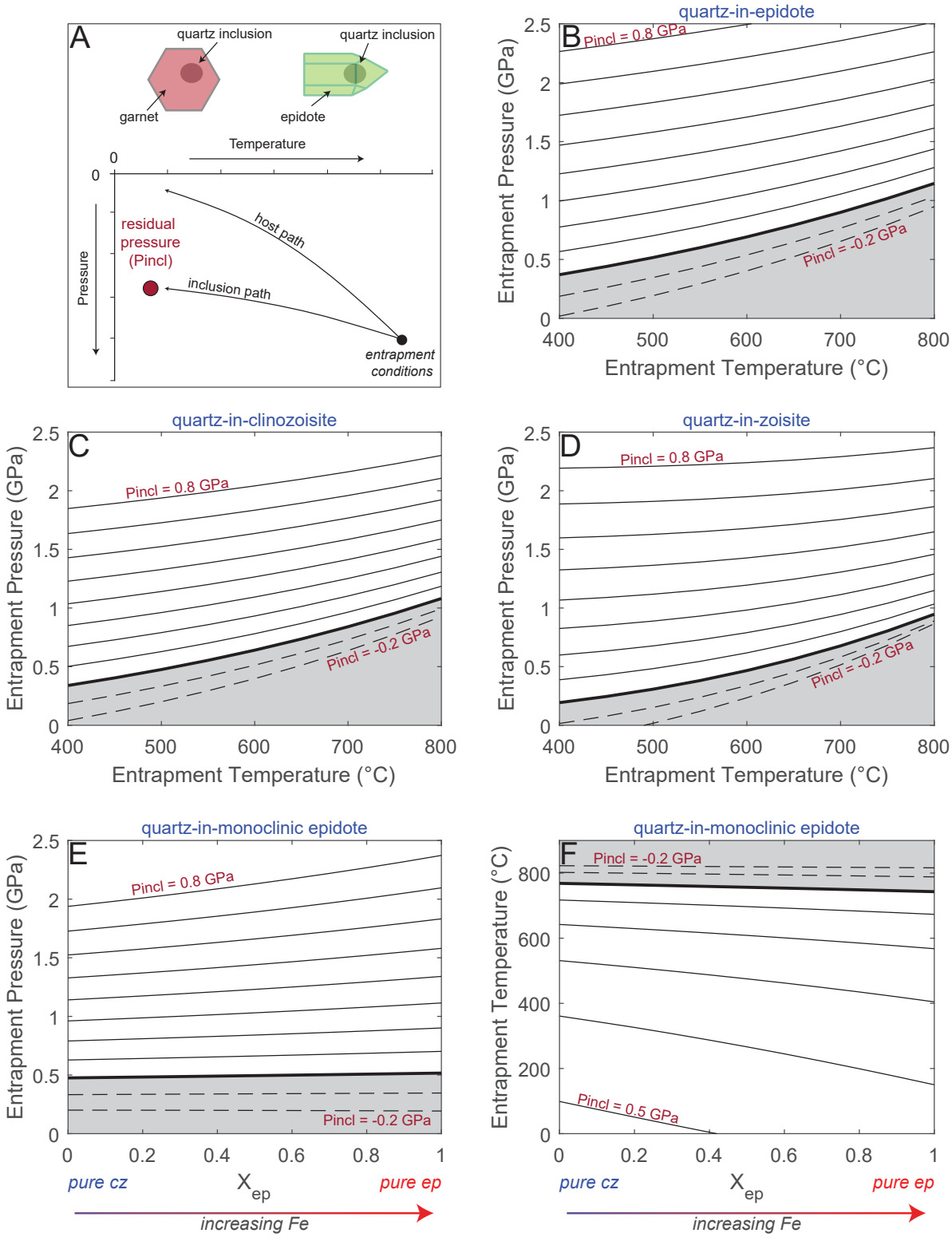

This is a preprint, the final version is subject to change, of the American Mineralogist (MSA)
Cite as Authors (Year) Title. American Mineralogist, in press.
DOI: https://doi.org/10.2138/am-2020-7379

Figure 2

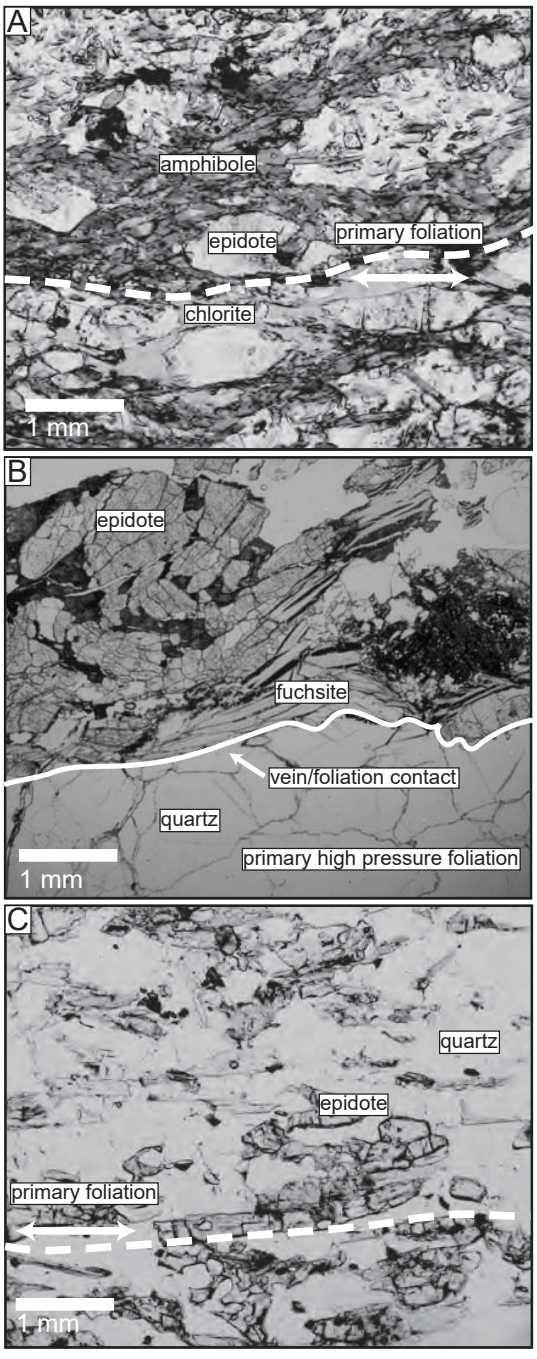

This is a preprint, the final version is subject to change, of the American Mineralogist (MSA)
Cite as Authors (Year) Title. American Mineralogist, in press.
DOI: https://doi.org/10.2138/am-2020-7379

Figure 3

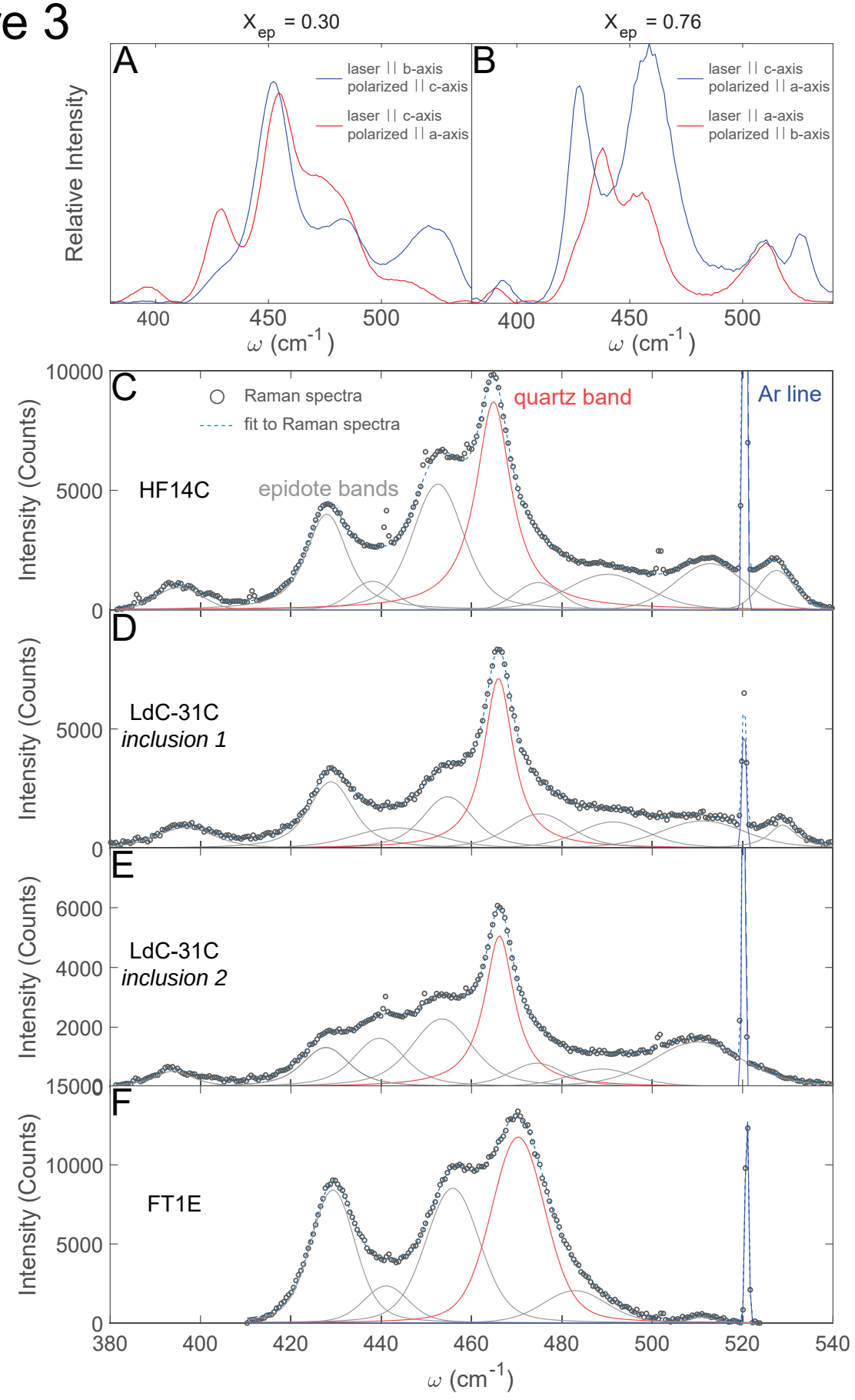

This is a preprint, the final version is subject to change, of the American Mineralogist (MSA)
Cite as Authors (Year) Title. American Mineralogist, in press.
DOI: https://doi.org/10.2138/am-2020-7379

Figure 4

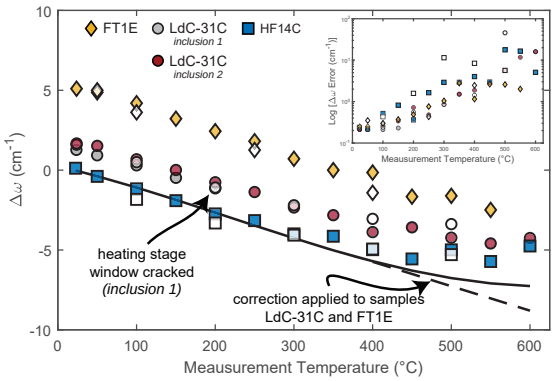

This is a preprint, the final version is subject to change, of the American Mineralogist (MSA)
Cite as Authors (Year) Title. American Mineralogist, in press.
DOI: https://doi.org/10.2138/am-2020-7379

Figure 5

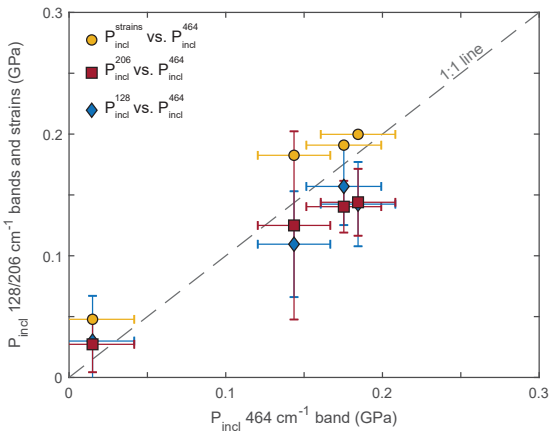

This is a preprint, the final version is subject to change, of the American Mineralogist (MSA)
Cite as Authors (Year) Title. American Mineralogist, in press.
DOI: https://doi.org/10.2138/am-2020-7379

Figure 6

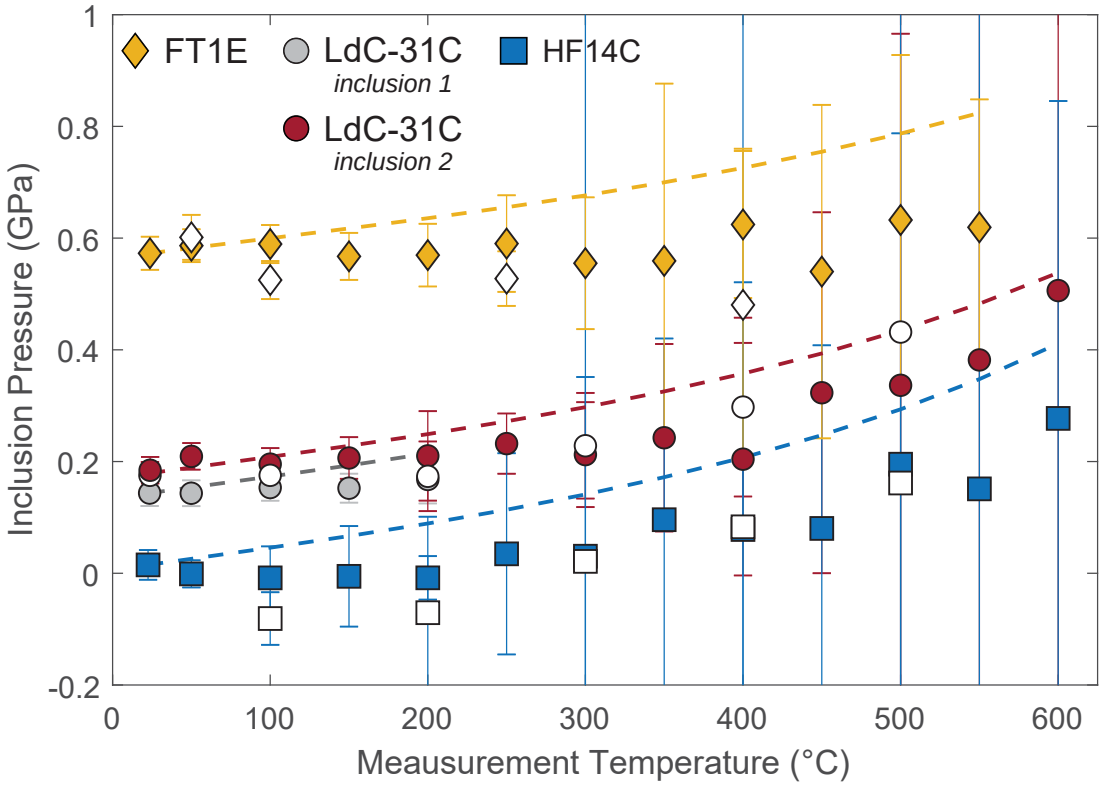

This is a preprint, the final version is subject to change, of the American Mineralogist (MSA)
Cite as Authors (Year) Title. American Mineralogist, in press.
DOI: https://doi.org/10.2138/am-2020-7379

Figure 7